



저작자표시-비영리-변경금지 2.0 대한민국

이용자는 아래의 조건을 따르는 경우에 한하여 자유롭게

- 이 저작물을 복제, 배포, 전송, 전시, 공연 및 방송할 수 있습니다.

다음과 같은 조건을 따라야 합니다:



저작자표시. 귀하는 원저작자를 표시하여야 합니다.



비영리. 귀하는 이 저작물을 영리 목적으로 이용할 수 없습니다.



변경금지. 귀하는 이 저작물을 개작, 변형 또는 가공할 수 없습니다.

- 귀하는, 이 저작물의 재이용이나 배포의 경우, 이 저작물에 적용된 이용허락조건을 명확하게 나타내어야 합니다.
- 저작권자로부터 별도의 허가를 받으면 이러한 조건들은 적용되지 않습니다.

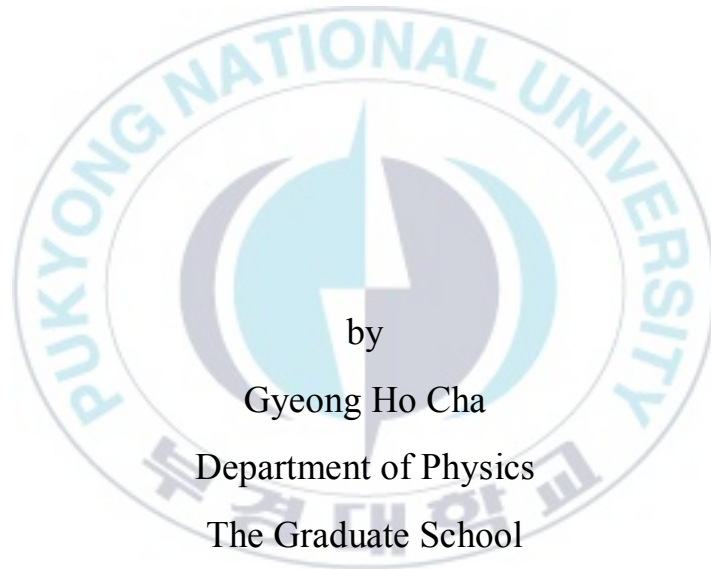
저작권법에 따른 이용자의 권리는 위의 내용에 의하여 영향을 받지 않습니다.

이것은 [이용허락규약\(Legal Code\)](#)을 이해하기 쉽게 요약한 것입니다.

[Disclaimer](#)

Thesis of the Degree of Master of Physics

First-Principles Study of Li Ion  
Diffusion in Lithium Oxythioborate  
Halide Glass Solid Electrolyte



by

Gyeong Ho Cha

Department of Physics

The Graduate School

Pukyong National University

August, 2022

First-Principles Study of Li Ion Diffusion  
in Lithium Oxythioborate Halide Glass  
Solid Electrolyte

(리튬 옥시오보레이트 할라이드계  
유리질 고체 전해질의 리튬이온  
확산의 제일원리연구)

Advisor : Prof. Sung Chul Jung

by

Gyeong Ho Cha

A thesis submitted in partial fulfillment of the requirements  
for the degree of Master of Physics

Department of Physics, The Graduate School,

Pukyong National University

First-Principles Study of Li Ion Diffusion in Lithium  
Oxythioborate Halide Glass Solid Electrolyte

A dissertation

by

Gyeong Ho Cha

Approved by:



---

(Chairman) Jisang Hong



---

(Member) Bo Ram Lee



---

(Member) Sung Chul Jung

August 26, 2022

# Contents

## List of Table and Figures

### Abstract

1. Introduction	1
2. Theory	4
2.1. Density functional theory (LDA and GGA).....	4
2.2. Plane-wave pseudopotential method .....	7
2.3. Projector augmented wave (PAW) method.....	9
3. Computational details	10
4. Results & discussion	12
4.1. LIBOSS structure.....	12
4.2. Radial distribution functions (RDFs) and coordination numbers (CNs) .....	14
4.3. Diffusivity analysis .....	20
4.4. Bader charge and diffusion trajectory.....	26
4.5. H <sub>2</sub> S gas formation.....	33
5. Conclusion	36
Reference	37

## List of Table and Figures

<b>Fig. 1.</b> LIBOSS ( $\text{Li}_{1.05}\text{B}_{0.5}\text{Si}_x\text{O}_{2x}\text{S}_{1.05}\text{I}_{0.45}$ ) glasses with (a) $x = 0$ , (b) 0.25, (c) 0.5, and (d) 1.0. ....	12
<b>Fig. 2.</b> RDFs of the atomic pairs in the LIBOSS glasses obtained from AIMD simulations for 3 ps at $T = 300$ K. ....	15
<b>Fig. 3.</b> CNs of atoms in the LIBOSS glasses. ....	16
<b>Fig. 4.</b> RDFs of the atomic pairs in the LIBOSS glasses obtained from the AIMD simulations for 3 ps at $T = 300$ K. ....	17
<b>Table 1</b> CNs of atoms in the LIBOSS glasses. ....	18
<b>Fig. 5.</b> $d_{\text{ms}}$ of Li ions in the LIBOSS glasses. ....	21
<b>Table 2</b> Diffusion properties of Li ions in the LIBOSS glasses. ....	22
<b>Table 3</b> Diffusion properties of Li ions in the LIBOSS ( $x = 0$ ) glasses with and without crystalline LiI. ....	22
<b>Fig. 6.</b> (a) $\ln D$ of Li ions as a function of inverse temperature in the LIBOSS glasses. (b) $D$ and (c) $\sigma$ of Li ions as a function of $\text{SiO}_2$ content in the LIBOSS glasses at $T = 300$ K. ....	23
<b>Fig. 7.</b> $d_{\text{ms}}$ of Li ions in the LIBOSS ( $x = 0$ ) glasses (a) with and (b) without crystalline LiI. (c) $\ln D$ of Li ions in the LIBOSS ( $x = 0$ ) glasses with and without crystalline LiI. ....	24

<b>Table 4</b> Li–A distances ( $d$ ), Bader charges ( $Q$ ), and their combinations to evaluate the electrostatic interactions in the LIBOSS glass with $x = 0.25$ . ....	26
<b>Fig. 8.</b> (a) $d_{ms}$ of fast- and slow-moving Li ions in the LIBOSS glass with $x = 0.25$ at $T = 900$ K. (b) CNs of the fast and slow Li ions over a period of 30 ps. (c) Trajectory of the fast Li ion over a period of 4 ps (11.5–15.5 ps). ....	30
<b>Table 5</b> $CN_{Li-A}$ and $d_{Li-A}$ of the fast Li ion in Fig. 5(a), obtained over a partial period of 1 ps (13.1–14.1 ps) and a full period of 30 ps in the AIMD simulation of the LIBOSS ( $Li_{1.05}B_{0.5}Si_xO_{2x}S_{1.05}I_{0.45}$ ) glass with $x = 0.25$ for 30 ps at $T = 900$ K. ....	31
<b>Fig. 9.</b> Formation energy of $H_2S$ from LIBOSS, defined as $E_f = [E(LIBOSS; N_S - 2) + 2E(H_2S) + 2E(O_2) - E(LIBOSS; N_S) - 2E(H_2O)]/2$ . ....	35

First-Principles Study of Li Ion Diffusion in Lithium Oxythioborate Halide Glass Solid Electrolyte

Gyeong Ho Cha

Department of Physics, The Graduate School  
Pukyong National University

Abstract

Due to their absence of grain boundaries that limit Li ion transport and provoke dendritic growth, glass materials are considered promising solid electrolytes for all-solid-state lithium batteries. However, the understanding of ion transport in glassy solid electrolytes is limited because of their disordered structure. In this study, the Li ion diffusion mechanism in lithium oxythioborate halide ( $\text{Li}_2\text{S}-\text{B}_2\text{S}_3-\text{LiI}-\text{SiO}_2$ ) quaternary glasses with different  $\text{SiO}_2$  contents is reported. Oxygen in the glass can increase and decrease Li ion conductivity by disrupting local LiI crystals and forming strong bonds with Li ions. This conductivity is determined by the competition of the two effects of oxygen at each  $\text{SiO}_2$  content, causing a maximum conductivity of  $14.6 \text{ mS cm}^{-1}$  in the  $30\text{Li}_2\text{S}\cdot 25\text{B}_2\text{S}_3\cdot 45\text{LiI}\cdot 25\text{SiO}_2$  composition, comparable to that of a liquid electrolyte of about  $10 \text{ mS cm}^{-1}$ . Li ion hopping easily occurs in cation-rich environments, as the cations facilitate the breaking of the bonds of Li with

anions, especially oxygen, by attracting the anions around Li, which is suggested to be the cation-assisted Li ion diffusion mechanism. This study suggests that controlling the oxygen:sulfur ratio in glassy solid electrolytes is key to promoting Li ion diffusion while minimizing immobilized Li ions and improving moisture stability.



# 1. Introduction

Among all-solid-state batteries (ASSBs), solid electrolytes are in an important position to overcome the potential safety risks and energy density limits of conventional lithium-ion batteries (LIBs) [1–5]. LIBs that use liquid electrolytes are vulnerable to fire and one of the causes of the fire is flammable liquid electrolytes [5–9]. Replacing these flammable liquid electrolytes, the safety issues of batteries can be further solved, and the ASSBs can provide higher energy densities compared to current LIBs [6]. Other advantages of substitution include high ionic conductivity, interfacial chemical stability, and high resistance to dendrite growth [6,10–12].

Of these, ionic conductivity has a significant impact on the performance of solid electrolyte (SE). In general, the ionic conductivity of ASSB at room temperature is lower than that of LIB ( $10 \text{ mS cm}^{-1}$ ) [10], but it is essential to approach the value of liquid electrolyte to replace liquid electrolyte. Among the investigated SE, that is, oxides, sulfides, and halides, sulfides such as  $\text{Li}_2\text{S-P}_2\text{S}_5$  ( $70\text{Li}_2\text{S}\cdot 30\text{P}_2\text{S}_5$ ) [13],  $\text{Li}_{10}\text{GeP}_2\text{S}_{12}$  [14], and  $\text{Li}_{9.54}\text{Si}_{1.74}\text{P}_{1.44}\text{S}_{11.7}\text{Cl}_{0.3}$  [15] satisfy this ionic conductivity.

The reason why the ionic conductivity of sulfide SE is higher than that of other SEs is that the interaction between  $\text{Li}^+$  ions and anions is weakened due to the polarization of sulfur [16,17]. In addition, sulfide SE has a low grain

boundary resistance, which facilitates ion transport [10,16,18]. However, sulfide SE produces very toxic H<sub>2</sub>S gas when exposed to humid air, so sulfide SE requires further treatment to reduce H<sub>2</sub>S production [10,18]. On the other hand, Oxide SE has high moisture resistance, electrochemical and mechanical stability, but the conductivity is about 10<sup>-3</sup> S cm<sup>-1</sup> [10,19,20], which is lower than sulfide SE. The addition of oxide SE with these advantages to sulfide SE can be a method to increase moisture resistance while maintaining ionic conductivity. Indeed, it has been reported that the addition of metal oxides such as Fe<sub>2</sub>O<sub>3</sub>, ZnO, and Bi<sub>2</sub>O<sub>3</sub> to the Li<sub>3</sub>PS<sub>4</sub> glass electrolyte reduces the generation of H<sub>2</sub>S gas [21].

Recently, kaup et al. [22] reported lithium oxythioborate halide (Li<sub>2</sub>S-B<sub>2</sub>S<sub>3</sub>-LiI-SiO<sub>2</sub>; LIBOSS) of a glass electrolyte with a maximum conductivity of 2 mS cm<sup>-1</sup> and a low H<sub>2</sub>S gas emission when exposed to moisture. Given that LIBOSS is an oxysulfide glass and not a pure sulfide glass, the reported conductivity at room temperature is quite high. In addition, although LIBOSS glasses contain large amounts of oxygen, they have higher ionic conductivity across a wide SiO<sub>2</sub> content range than lithium thioborate halide (Li<sub>2</sub>S-B<sub>2</sub>S<sub>3</sub>-LiI) glass without oxygen. Furthermore, because of their glassy structure, LIBOSS glasses have no grain boundaries, which facilitates fast Li ion transport and does not trigger dendrite growth at grain boundaries [23,24]. Due to the absence of grain boundaries, many studies have recently investigated glassy solid electrolytes for ASSBs [22–31]. However, understanding the roles of glass elements on Li ion

transport in glass materials such as LIBOSS is challenging because the ion conduction mechanism in glassy structures is usually elusive due to the disordered amorphous nature of these structures.

In this study, we investigated the Li ion diffusion mechanism in LIBOSS glasses with different SiO<sub>2</sub> contents using density functional theory (DFT) calculations and ab initio molecular dynamics (AIMD) simulations. The structures of LIBOSS glasses constructed using AIMD simulations were investigated by analyzing radial distribution functions (RDFs), coordination numbers (CNs), and Bader charges. The analyzed results were used to interpret the bell-shaped curve of the Li ion conductivity as a function of SiO<sub>2</sub> content, which exhibits the highest value of 14.6 mS cm<sup>-1</sup> in the 30Li<sub>2</sub>S·25B<sub>2</sub>S<sub>3</sub>·45LiI·25SiO<sub>2</sub> composition. Analysis of the movements of fast- and slow-moving Li ions at  $T = 900$  K offers a detailed picture of Li ion motion in LIBOSS glasses, which leads us to suggest the cation-assisted Li ion diffusion mechanism. The presence of SiO<sub>2</sub> in LIBOSS glasses turns out to increase the resistance to H<sub>2</sub>S formation and thus enhance moisture stability. This study also clarifies the roles of oxygen and sulfur in glassy solid electrolytes in terms of electrochemical performance. The calculation results provide atomic-level insights into the ion transport in glass materials and the design of high-performance glassy solid electrolytes for ASSBs.

## 2. Theory

### 2.1. Density functional theory (LDA and GGA)

Interpreting particles in the microscopic world requires solving the Schrödinger equation quantum-mechanically. A solid is a collection of many ( $\sim 10^{23}$ ) atoms, and understanding the physical and chemical properties of solids is very difficult. To solve this problem, Thomas-Fermi in 1927 calculated the kinetic, exchange, and correlation energies for a uniform electron density [32].

It is written as

$$E_m[n] = \int n(r)\varepsilon_m(n(r))dr \quad (1)$$

Here,  $m$  represents the type of energy, and  $\varepsilon$  denotes the energy density with respect to  $m$ .

Hamiltonian in a many-body problem can be written as

$$H = \widehat{E}_T + \widehat{E}_V + \widehat{E}_U \quad (2)$$

Here  $\widehat{E}_T$ ,  $\widehat{E}_V$  and  $\widehat{E}_U$  represents kinetic energy, external potential and coulomb energy respectively. This Hamiltonian satisfies the following equation

$$\widehat{H}|\Psi\rangle = E|\Psi\rangle \quad (3)$$

According to Hohenberg-Kohn's theorem, the Hamiltonian, the wave function, and the density function have a one-to-one correspondence, and the remainder except the external potential is always the same, ground state energy  $E_0$  can be calculated through transformation, and it can be obtained as follows

through Equations (1), (2), and (3) [33,34].

$$E_0[\rho] = E_T[\rho] + E_V[\rho] + E_U[\rho] \quad (4)$$

Where  $\rho$  is the electron density. And  $E_V[\rho]$  can be written as

$$E_V[\rho] = \int \rho(r)V(\rho(r))dr \quad (5)$$

$V$  can be found by the Hohenberg-Kohn theorem. The remaining terms are pure kinetic energy without interaction and interaction between electrons, and the interaction between electrons can be summarized as follows through Khon-Sham approximation, leaving only electrical interactions.

$$E_0[\rho] = E_T[\rho] + \frac{1}{2} \int \int \frac{\rho(\mathbf{r})\rho(\mathbf{r}')}{|\mathbf{r} - \mathbf{r}'|} d\mathbf{r}d\mathbf{r}' + \int \rho(\mathbf{r})V(\rho(\mathbf{r}))d\mathbf{r} \quad (6)$$

$$+ E_{xc}[\rho]$$

Here,  $E_{xc}[\rho]$  is an exchange-correlation potential, meaning that the exact value is unknown. If only this value is known,  $E_0[\rho]$  can be known. Therefore,  $E_0[\rho]$  can be obtained by approximating this  $E_{xc}[\rho]$ .

In 1965, Khon and Sham proposed Local Density Approximation (LDA) by approximating that the electron density when viewed locally is uniform. In this approximation,  $E_{xc}[\rho]$  for a uniform electron density was obtained as follows through Equation (1).

$$E_{xc}^{LDA}[\rho] = \int \rho(r) \varepsilon_{xc}(\rho(r))dr \quad (7)$$

Here, since  $\varepsilon_{xc}(\rho)$  is composed of electron density, only a uniform electron density can obtain  $E_0[\rho]$  through  $\rho(r)$ .

However, in real systems, the density changes with space. To compensate for this, a more accurate approximation can be made by adding a gradient term. These approximations are called generalized gradient approximations (GGAs) [35] and are written as

$$E_{xc}^{GGA}[\rho] = \int \rho(r) \varepsilon_{xc}(\rho(r), \nabla \rho(r)) dr \quad (8)$$

GGA doesn't always guarantee better results. In covalent bonds or weakly bonded systems, GGAs generally perform better.

Putting the equations together, the Schrödinger equation is as follows, which is called the Kohn-Sham equation.

$$\left( -\frac{1}{2} \nabla^2 + V_{ext}(r) + \int \frac{\rho(r')}{|\mathbf{r} - \mathbf{r}'|} d\mathbf{r}' + V_{xc}(r) \right) \psi_i(r) = \varepsilon_i \psi_i(r) \quad (9)$$

Here,  $\rho(r)$  is a function of the density of electrons, so it can be expressed as

$$\rho(r) = \sum_{i=1}^N |\psi_i(r)|^2 \quad (10)$$

Since  $V_{xc}$  is a potential, it becomes

$$V_{xc}(r) = \frac{\delta E_{xc}[\rho]}{\delta \rho(r)} \quad (11)$$

By substituting Equation (11) into Equation (9), the result is as follows.

$$\begin{aligned} & \left( -\frac{1}{2} \nabla^2 + V_{ext}(r) + \int \frac{\rho(r')}{|\mathbf{r} - \mathbf{r}'|} d\mathbf{r}' + \frac{\delta E_{xc}[\rho]}{\delta \rho(r)} \right) \psi_i(r) \\ & = \varepsilon_i \psi_i(r) \end{aligned} \quad (12)$$

Here, energy can be obtained by substituting Equation (7) or Equation (8) for  $E_{xc}$  alone and solving the Schrödinger equation.

## 2.2. Plane wave pseudopotential method

Electrons in solids are largely divided into core electrons and valence electrons. Valence electrons contribute to interactions between atoms, but core electrons exist around the nucleus in a closed shell. Valence electrons occupy a more important place in research than core electrons because they determine the chemical properties of matter. Also, since the core electrons block the charge of the nucleus, the potential felt by the valence electrons is lower than that of the core electrons. This fast oscillation of the core electron is explained by a very large number of plane waves, which greatly increases the computational complexity. Accordingly, Hamann, Schlüter and Chiang devised a method for generating pseudo potentials based on all-electron calculations of the potentials and wave functions [36]. First, by setting a plane wave, the periodic function  $u_{nk}(r)$  is extended as follows.

$$u_{nk}(\mathbf{r}) = \sum_G C_{nk,G} e^{i(G \cdot \mathbf{r})} \quad (13)$$

where the sum is the value on the reciprocal lattice vector  $G$ . Therefore, the electronic wave function can be written as

$$\varphi_{nk}(\mathbf{r}) = \sum_G C_{nk,G} e^{i(G \cdot \mathbf{r})} \quad (14)$$

This electronic wave function can be expressed as the sum of plane wave bases. Since this Fourier series is infinite, we cannot work with computational

calculation, so we have to limit the number of plane waves. The number of plane waves can be limited by placing an upper limit on the kinetic energy of plane waves. This boundary is called  $E_{cut}$ , and only plane waves that satisfy the following conditions need to be calculated.

$$\frac{|k + G|^2}{2} < E_{cut} \quad (15)$$

However, in a system with many electrons, it is still difficult to calculate. In the pseudo potential approximation, the core electron is removed and the strong ionic potential is replaced by a relatively weak pseudo potential wave function ( $\psi_{pseudo}$ ) acting on the real valence wave function ( $\psi$ ), which simplifies the action of the core electron ( $V_{pseudo}$ ).  $V_{pseudo}$  and  $\psi_{pseudo}$  are generated in the same way as actual potentials and wave functions. All nodes of the pseudo potential at the core are removed, but the norm is preserved. Since the node of the core is removed, the number of plane waves required to explain the wave function at the core is reduced. For this reason, the plane-wave pseudo potential method was applied.

### 2.3. Projector augmented wave (PAW) method

A disadvantage of the pseudo potential method is that information on wave functions close to the nucleus is removed. This lack of information can affect the results when calculating hyperfine parameters, electric field gradients, etc. projector augmented wave (PAW) calculates all electronic properties by replacing these core wave functions with smooth wave functions [37]. When PAW is applied, the total energy is divided into two parts as follows.

$$E = \tilde{E} + \sum_a \Delta E^a \quad (16)$$

Here,  $\tilde{E}$  is the energy calculated by the smooth function, and  $\Delta E^a$  is the energy around the nucleus.  $\tilde{E}$  can be expanded as follows.

$$\tilde{E} = T_s[\{\tilde{\psi}_n\}] + U'_H[\tilde{\rho}] + E_{xc}[\tilde{n}] \quad (17)$$

This equation is similar to the structure of general energy, but it can better explain the core electron because  $\tilde{\rho}$  and  $\tilde{n}$ , which are derived from the smooth function, substituted  $\rho$  and  $n$ .

### 3. Computational details

In this study, DFT calculations were carried out using Vienna ab initio simulation package (VASP) [38]. The Perdew-Burke-Ernzerhof (PBE) exchange and correlation functionals [34], and the projector augmented wave (PAW) method [37] were used. The plane-wave energy cutoff was set to 374.3 eV.  $1s^22s^1$  for Li,  $2s^22p^1$  for B,  $2s^22p^4$  for O,  $3s^22p^2$  for Si,  $3s^23p^4$  for S, and  $5s^25p^5$  for I were considered as the valence electron configurations.  $\text{Li}_{1.05}\text{B}_{0.5}\text{Si}_x\text{O}_{2x}\text{S}_{1.05}\text{I}_{0.45}$  ( $x = 0, 0.25, 0.5,$  and  $1.0$ ) was used as the composition of LIBOSS glasses considering the  $\text{Li}_2\text{S}:\text{B}_2\text{S}_3:\text{LiI}$  ratio of 30:25:45 reported in the experimental study [22]. The LIBOSS glass structures were simulated by a tetragonal supercell for  $x = 0$  and cubic supercells for  $x = 0.25, 0.5,$  and  $1.0$ . The LiI crystals were reported to be partially formed in the LIBOSS glass with  $x = 0$  [22], which led us to make the LiI crystal within the supercell using the tetragonal supercell for  $x = 0$ . The total numbers of atoms used in the supercells are 217, 271, 322, and 363 for  $x = 0, 0.25, 0.5,$  and  $1.0,$  respectively. A  $1 \times 1 \times 1$   $k$ -point mesh was employed for Brillouin-zone integrations.

AIMD simulations were used to generate glass structures. The equations of motion were integrated with the Verlet algorithm using a time step of 1 fs. The temperature was controlled by velocity rescaling and a canonical ensemble using a Nosé–Hoover thermostat. The LIBOSS glass structures were

constructed using the liquid-quench method. The Li, B, O, Si, S, and I atoms were randomly distributed in the tetragonal ( $x = 0$ ) and cubic ( $x = 0.25, 0.5,$  and  $1.0$ ) supercells, except for 32 Li and 32 I atoms placed at bulk positions to make the LiI crystal for  $x = 0$ . These initial structures were heated up to 4000 K at a heating rate of  $1 \text{ K fs}^{-1}$ , equilibrated for 3–6 ps at 4000 K, and then quenched to 300 K at a cooling rate of  $1 \text{ K fs}^{-1}$ . The quenched structures were equilibrated for 5 ps at 300 K. For  $x = 0$ , the volume of the last structure of the equilibration step at 300 K was determined by optimizing the  $c$ -axis of the tetragonal supercell using static DFT calculations. For  $x = 0.25, 0.5,$  and  $1.0$ , three structures were taken every 1 ps in the last 2 ps of the equilibration step at 300 K, and their volumes were determined by optimizing the cubic supercells using static DFT calculations. The final volume for each  $x$  ( $x = 0.25, 0.5,$  and  $1.0$ ) was determined by averaging the volumes of the three structures. A higher plane-wave energy cutoff of 648.7 eV was used in the volume-determination processes to avoid the Pulay stress problem [39] caused by the volume change of the cell. Finally, the LIBOSS structures were adjusted to the tetragonal ( $x = 0$ ) and cubic ( $x = 0.25, 0.5,$  and  $1.0$ ) supercells with the determined volumes and again equilibrated for 5 ps at 300 K. RDFs and CNs of the structures obtained from this equilibration step were analyzed using rigorous investigation of networks generated using simulations (RINGS) code.

## 4. Result & discussion

### 4.1. LIBOSS structure

In this study, we mixed  $\text{Li}_2\text{S}$ ,  $\text{B}_2\text{S}_3$ , and  $\text{LiI}$  in a ratio of 30:25:45 to prepare three structures in which  $\text{LiI}$  is crystallized, partially crystallized, and amorphous [22,40,41]. Among them, the most stable structure is a crystallized structure, which has a unit energy 0.10 eV lower than that of other structures (Fig. 1(a)). These results are consistent with the results of actual experiments [22]. After that,  $\text{SiO}_2$  was added to  $30\text{Li}_2\text{S}\cdot 25\text{B}_2\text{S}_3\cdot 45\text{LiI}$  to make the models of  $x = 0.25$ ,  $x = 0.5$ , and  $x = 1.0$  with the ratio of LIBOSS ( $\text{Li}_{1.05}\text{B}_{0.5}\text{Si}_x\text{O}_{2x}\text{S}_{1.05}\text{I}_{0.45}$ ) reported in the paper (Fig. 1(b)–(d)) [22].

The addition of  $\text{SiO}_2$  to  $\text{Li}_2\text{S}\text{--}\text{B}_2\text{S}_3\text{--}\text{LiI}$  glass leads to the formation of LIBOSS ( $\text{Li}_{1.05}\text{B}_{0.5}\text{Si}_x\text{O}_{2x}\text{S}_{1.05}\text{I}_{0.45}$ ) glass. The  $\text{LiI}$  crystals start to dissolve with even a small amount of  $\text{SiO}_2$  ( $x = 0.125$ ) and completely dissolve with a larger amount ( $x = 0.25$ ) [22].

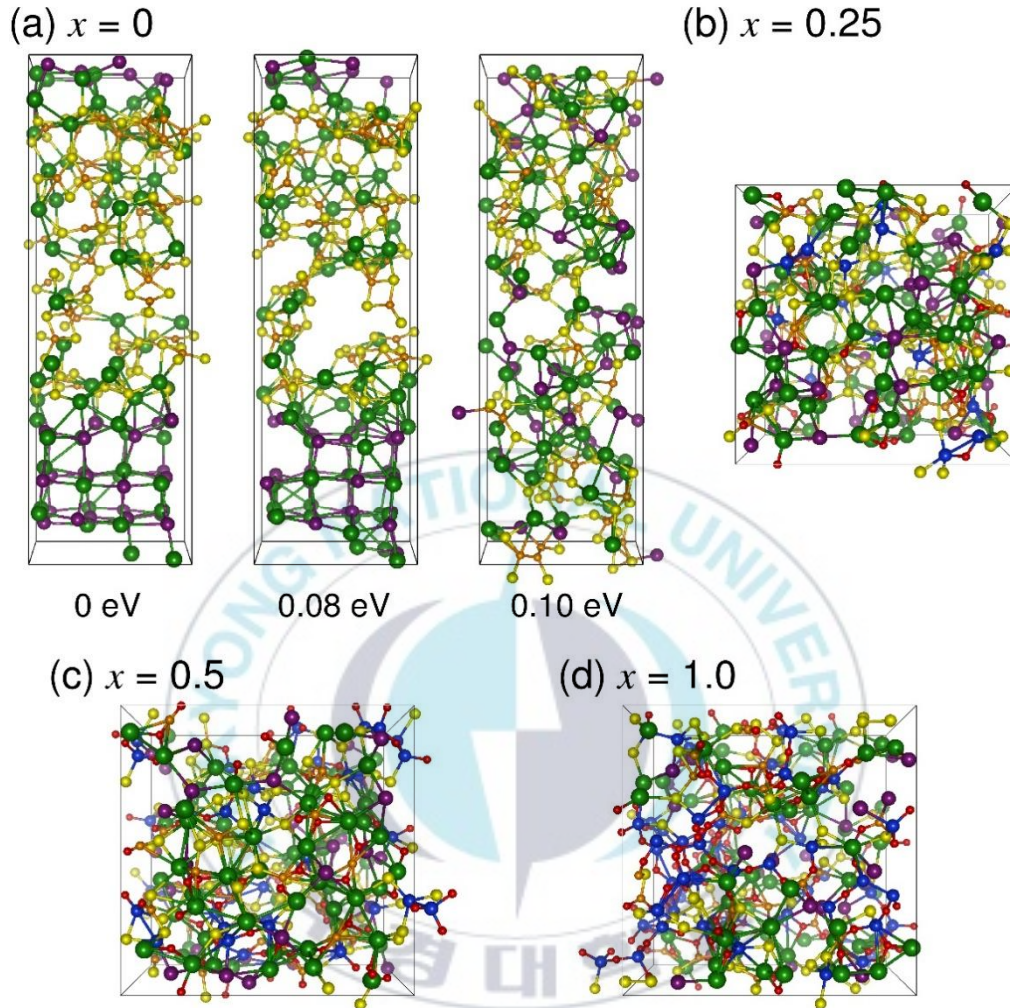


**Fig. 1.** LIBOSS ( $\text{Li}_{1.05}\text{B}_{0.5}\text{Si}_x\text{O}_{2x}\text{S}_{1.05}\text{I}_{0.45}$ ) glasses with (a)  $x = 0$ , (b) 0.25, (c) 0.5, and (d) 1.0. The green, orange, red, blue, yellow, and purple spheres represent the Li, B, O, Si, S, and I atoms, respectively. For  $x = 0$ , three glass models, one containing crystalline LiI, one containing partially collapsed LiI, and one containing fully collapsed LiI, are shown with numbers representing the relative energies per  $\text{Li}_{1.05}\text{B}_{0.5}\text{S}_{1.05}\text{I}_{0.45}$  formula unit.

## 4.2. Radial distribution functions (RDFs) and coordination numbers (CNs)

RDFs analysis was performed to confirm the change in the average bonding distance of each element according to the input ratio of  $\text{SiO}_2$ . As a result, there was no peak when  $r > 3 \text{ \AA}$  or more, and the peak appeared widely in the bonding between Li–Li, Li–B, and Li–Si. The absence of such a long-range order indicates the amorphous nature of LIBOS. The peak positions for Li–S and B–S pairs are 2.45 to 2.51 and 1.82 to 1.87  $\text{\AA}$  at  $x = 0, 0.25, 0.5,$  and  $1.0,$  respectively, with a small deviation of 0.05 to 0.06  $\text{\AA}$  (Fig.2). However, Li–I, Li–Li, and Li–B show significant changes in the addition of  $\text{SiO}_2$ . Li–I, Li–Li, and Li–B were 2.86, 4.34, 3.40  $\text{\AA}$  at  $x = 0$  and decreased relative to  $x = 0$  to 2.73, 3.12, and 2.84  $\text{\AA}$  at  $x = 1.0$ . In order to confirm that the cause of this decrease is due to the input of  $\text{SiO}_2$ , the RDF having a crystallization structure of  $x = 0$  and the RDF having an amorphous structure were compared. As a result, it can be seen that, in the case of Li–I, the crystallization of Li–I had a large effect, but in the case of Li–Li and Li–B, the structural change by the addition of  $\text{SiO}_2$  was the effect. Additionally, CNs between atoms in the LIBOSS glass were identified. Among them,  $\text{CN}_{\text{Li-S}}, \text{CN}_{\text{Li-I}},$  and  $\text{CN}_{\text{B-S}}$  decrease by 0.89, 1.13, and 1.87, respectively, as  $x$  increases from 0 to 1.0 (Fig.3 and Table 1). This change is due to the preference for O atoms to attach to Li atoms and B atoms due to the input

of SiO<sub>2</sub>. This is explained by 0.62, and 0.83 increases in CN<sub>Li-O</sub>, and CN<sub>B-O</sub> when  $x$  increases from 0.25 to 1.0. The radial distribution functions (RDFs) for the Li-S, Li-I, Li-Li, Li-B, and B-S pairs in the LIBOSS glasses with  $x = 0$  and 1.0 were displayed in Fig. 4. For  $x = 0$ , the RDFs in the glasses with and without crystalline LiI were also displayed. The peak position of the Li-I pair shifts downward by 0.13 Å from 2.86 Å for  $x = 0$  (with LiI) to 2.73 Å for  $x = 1.0$ . The shift of 0.13 Å in the Li-I distance is mainly due to the collapse of LiI crystal in LIBOSS, because the Li-I peak position for  $x = 0$  (without LiI) is closer to that for  $x = 1.0$  than for  $x = 0$  (with LiI). The peak positions of the Li-Li and Li-B pairs shift downward by 0.56–1.22 Å from 4.34 and 3.40 Å for  $x = 0$  (with LiI), respectively, to 3.12 and 2.84 Å for  $x = 1.0$ , respectively. The shifts of 1.22 and 0.56 Å in the Li-Li and Li-B distances are mainly attributed to SiO<sub>2</sub>-induced structural changes, because the Li-Li and Li-B peak positions for  $x = 0$  (without LiI) are closer to those for  $x = 0$  (with LiI) than for  $x = 1.0$ .

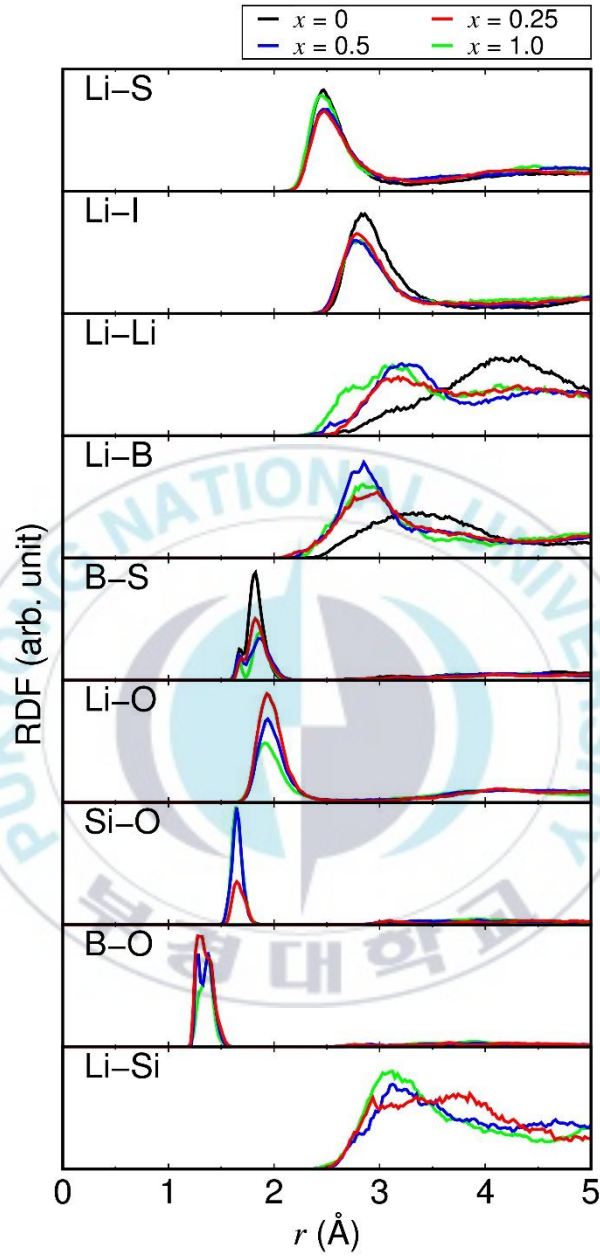


**Fig. 2.** Radial distribution functions (RDFs) of the atomic pairs in the LIBOSS ( $\text{Li}_{1.05}\text{B}_{0.5}\text{Si}_x\text{O}_{2x}\text{S}_{1.05}\text{I}_{0.45}$ ) glasses obtained from AIMD simulations for 3 ps at  $T = 300$  K.

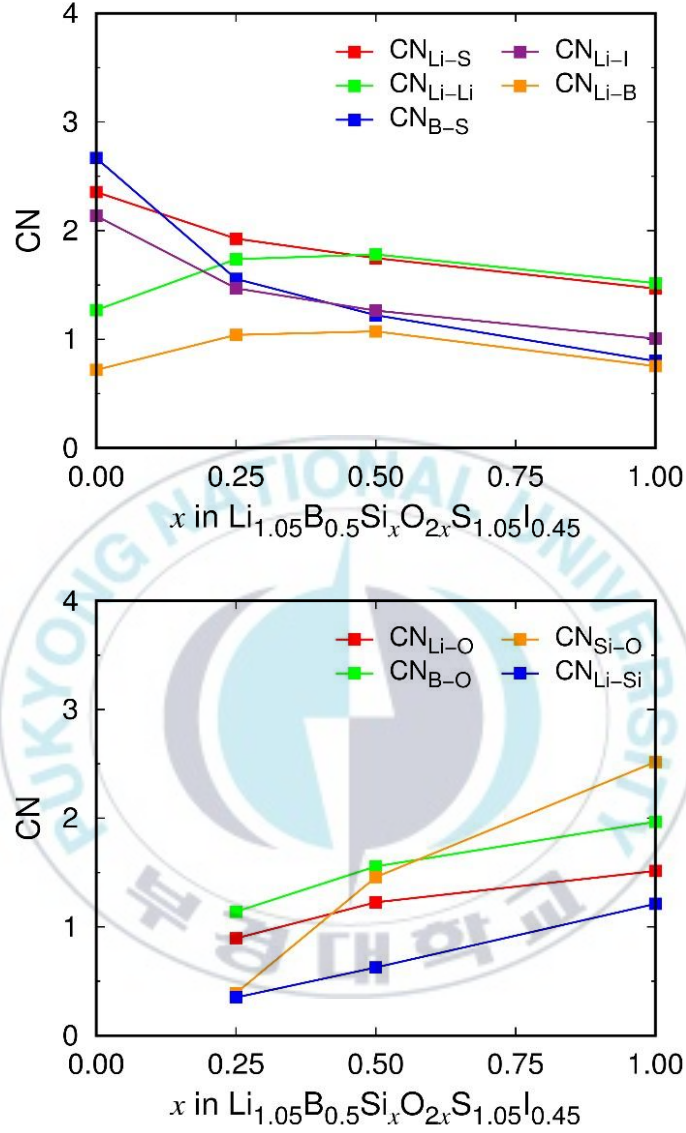


**Fig. 3.** Coordination numbers (CNs) of atoms in the LIBOSS ( $\text{Li}_{1.05}\text{B}_{0.5}\text{Si}_x\text{O}_{2x}\text{S}_{1.05}\text{I}_{0.45}$ ) glasses.  $\text{CN}_{\alpha-\beta}$  represents the number of  $\beta$  atoms around an  $\alpha$  atom. The bond cutoff distances are 3.3, 3.7, 3.7, 3.3, 2.5, 2.8, 2.5, 2.0, and 3.5 Å for the Li-S, Li-I, Li-Li, Li-B, B-S, Li-O, Si-O, B-O, and Li-Si pairs, respectively.

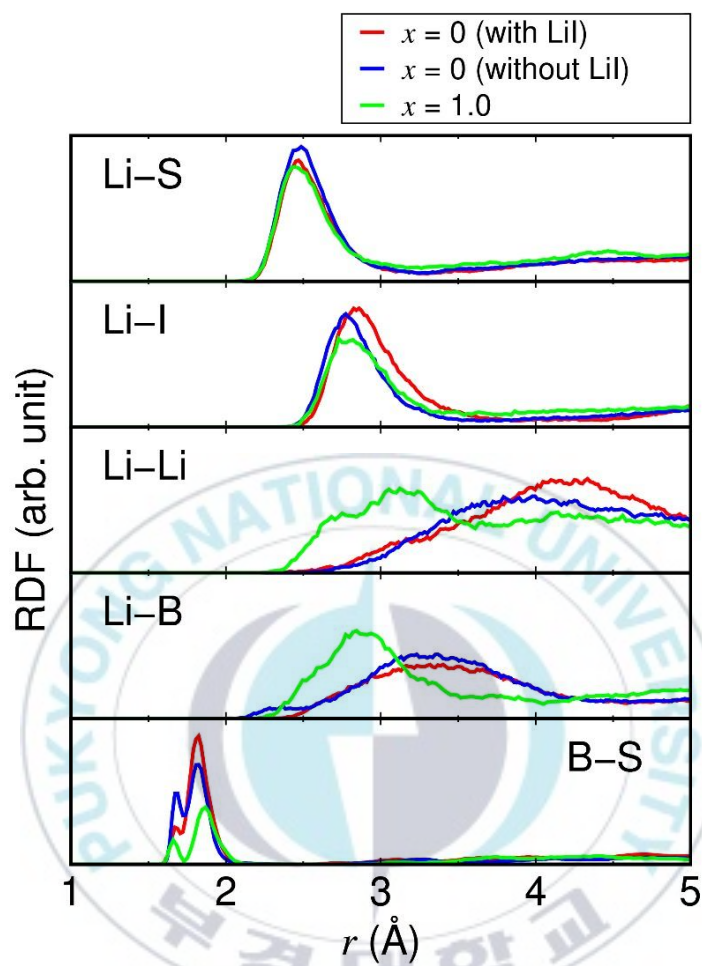


**Fig. 4.** Radial distribution functions (RDFs) of the atomic pairs in the LIBOSS ( $\text{Li}_{1.05}\text{B}_{0.5}\text{Si}_x\text{O}_{2x}\text{S}_{1.05}\text{I}_{0.45}$ ) glasses obtained from the AIMD simulations for 3 ps at  $T = 300$  K.

**Table 1**

Coordination numbers (CNs) of atoms in the LIBOSS ( $\text{Li}_{1.05}\text{B}_{0.5}\text{Si}_x\text{O}_{2x}\text{S}_{1.05}\text{I}_{0.45}$ ) glasses.<sup>a</sup>

$\text{CN}_{\alpha-\beta}$	$x = 0$	$x = 0.25$	$x = 0.5$	$x = 1.0$
$\text{CN}_{\text{Li-S}}$	2.36	1.93	1.75	1.47
$\text{CN}_{\text{Li-I}}$	2.14	1.47	1.26	1.01
$\text{CN}_{\text{Li-Li}}$	1.27	1.74	1.78	1.52
$\text{CN}_{\text{Li-B}}$	0.72	1.04	1.07	0.75
$\text{CN}_{\text{B-S}}$	2.67	1.56	1.22	0.80
$\text{CN}_{\text{Li-O}}$		0.89	1.23	1.51
$\text{CN}_{\text{Si-O}}$		0.39	1.46	2.52
$\text{CN}_{\text{B-O}}$		1.14	1.56	1.97
$\text{CN}_{\text{Li-Si}}$		0.35	0.63	1.21

<sup>a</sup>  $\text{CN}_{\alpha-\beta}$  represents the number of  $\beta$  atoms around an  $\alpha$  atom. The bond cutoff distances are 3.3, 3.7, 3.7, 3.3, 2.5, 2.8, 2.5, 2.0, and 3.5 Å for the Li-S, Li-I, Li-Li, Li-B, B-S, Li-O, Si-O, B-O, and Li-Si pairs, respectively.

### 4.3. Diffusivity analysis

Li ion transport in LIBOSS glass at  $T = 300$  K was examined using AIMD simulation. To effectively obtain Li ion diffusivity ( $D$ ) at  $T = 300$  K, LIBOSS glasses at  $x = 0, 0.25, 0.5$  and  $1.0$  were simulated at  $T = 600, 700, 800$  and  $900$  K for 30 ps. In the LIBOSS glass with  $x = 0$ , the two inner layer atoms of the LiI crystal were kept in the bulk position to prevent the destruction of the crystalline LiI during simulations at these temperatures ( $\geq 600$  K). The mean-square displacement of Li ions at  $T = 600, 700, 800$  and  $900$  K was calculated as a function of  $t$ . The calculated dms curves are approximately linear for  $x = 0, 0.25, 0.5$  and  $1.0$  (Fig. 5). This linearity allowed us to determine the  $D$  values at  $T = 600, 700, 800$ , and  $900$  K using the Einstein relation  $D = \langle r^2(t) \rangle / 6t$ . where  $D$  is diffusivity and  $\langle r^2(t) \rangle$  is the mean-square displacement. The  $D$  values at  $T = 600, 700, 800$ , and  $900$  K were estimated using the Arrhenius law  $D = D_0 \exp(-E_D/k_B T)$  at  $T = 300$  K. where  $D_0$  is the pre-exponential factor,  $E_D$  is the activation energy for diffusion, and  $K_B$  is the Boltzmann constant. Arrhenius plots for  $x = 0, 0.25, 0.5$  and  $1.0$  show the linear change of  $\ln(D)$  with inverse temperature (Fig. 6(a)).

The calculated Li ion diffusivity in LIBOSS glass at  $T = 300$  K is  $3.0 \times 10^{-8}$ ,  $2.0 \times 10^{-7}$ ,  $1.5 \times 10^{-7} \text{ cm}^2 \text{ s}^{-1}$  at  $x = 0, 0.25, 0.5$  and  $1.0$ , respectively (Table 1 and Fig.6(b)). Using the Li ion diffusivity at  $T = 300$  K, the Li ion conductivity

( $\sigma$ ) was estimated based on the Nernst-Einstein relationship  $\sigma = DNq^2/k_B T$ , where  $N$  is the carrier density and  $q$  is the carrier charge. The Li ion conductivities were 2.5, 14.6, 9.8 and 7.4 mS cm<sup>-1</sup> at  $x = 0, 0.25, 0.5,$  and 1.0, respectively (Table 2), with the maximum at  $x = 0.25$  (Fig. 6(c)). The conductivity of 14.6 mS cm<sup>-1</sup> at  $x = 0.25$  is close to a value of about 10 mS cm<sup>-1</sup> for a conventional liquid electrolyte [10]. The calculated conductivity for each  $x$  differs from each experimental value (Table 2) by approximately one order. Nevertheless, the conductivity curve peaking at  $x = 0.25$  and decreasing as  $x$  deviates from 0.25 is in good agreement with that reported by Kaup et al. [22] (Fig. 6(c)). This suggests that the simulation model for LIBOSS glass is qualitatively valid.

For  $x = 0$ , the diffusivity calculation results in the LIBOSS glasses with and without crystalline LiI were also presented in Fig. 7 and Table 3. The structures of LIBOSS glasses with and without crystalline LiI were displayed in Fig. 1a. The LIBOSS glass with crystalline LiI is more stable by 0.1 eV per formula unit than that without crystalline LiI.

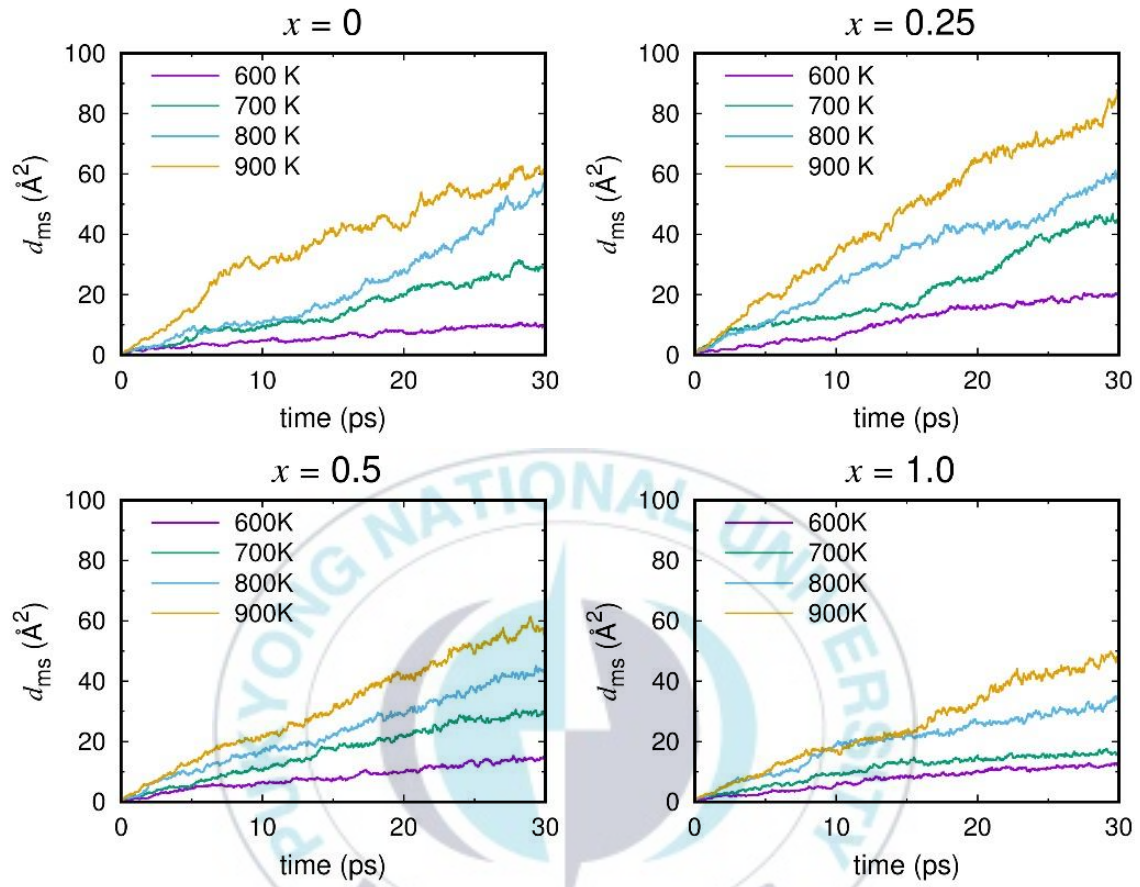


**Fig. 5.** Mean-square displacements ( $d_{ms}$ ) of Li ions in the LIBOSS ( $\text{Li}_{1.05}\text{B}_{0.5}\text{Si}_x\text{O}_{2x}\text{S}_{1.05}\text{I}_{0.45}$ ) glasses.

**Table 2**Diffusion properties of Li ions in the LIBOSS ( $\text{Li}_{1.05}\text{B}_{0.5}\text{Si}_x\text{O}_{2x}\text{S}_{1.05}\text{I}_{0.45}$ ) glasses.<sup>a</sup>

	$x$	$D_0$	$D$	$E_D$	$\sigma$
This work	0	$1.5 \times 10^{-3}$	$3.0 \times 10^{-8}$	0.28	2.5
	0.25	$7.8 \times 10^{-4}$	$2.0 \times 10^{-7}$	0.21	14.6
	0.5	$5.4 \times 10^{-4}$	$1.5 \times 10^{-7}$	0.21	9.8
	1.0	$3.8 \times 10^{-4}$	$1.4 \times 10^{-7}$	0.20	7.4
Ref [22].	0			0.35	0.53
	0.25			0.33	2.1
	0.5			0.35	1.0
	1.0			0.36	0.18

<sup>a</sup> $D_0$  ( $\text{cm}^2 \text{s}^{-1}$ ) is the pre-exponential factor,  $D$  ( $\text{cm}^2 \text{s}^{-1}$ ) is the diffusivity at  $T = 300$  K,  $E_D$  (eV) is the activation energy for diffusion, and  $\sigma$  ( $\text{mS cm}^{-1}$ ) is the conductivity at  $T = 300$  K.

**Table 3**Diffusion properties of Li ions in the LIBOSS ( $x = 0$ ) glasses with and without crystalline LiI

	$D_0$	$D$	$E_D$	$\sigma$
with LiI	$1.5 \times 10^{-3}$	$3.0 \times 10^{-8}$	0.28	2.5
without LiI	$8.2 \times 10^{-4}$	$7.9 \times 10^{-7}$	0.18	66.1

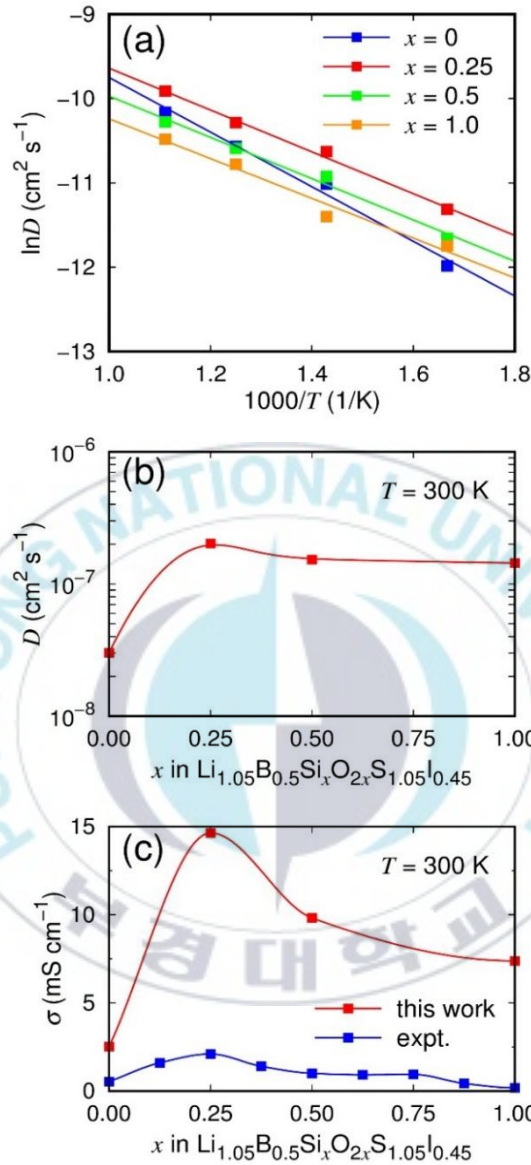


**Fig. 6.** (a) Logarithmic diffusivity ( $\ln D$ ) of Li ions as a function of inverse temperature in the LIBOSS ( $\text{Li}_{1.05}\text{B}_{0.5}\text{Si}_x\text{O}_{2x}\text{S}_{1.05}\text{I}_{0.45}$ ) glasses. (b) Diffusivity ( $D$ ) and (c) conductivity ( $\sigma$ ) of Li ions as a function of SiO<sub>2</sub> content in the LIBOSS glasses at  $T = 300 \text{ K}$ . In (c), the blue squares represent the conductivity reported in an experimental study [22].

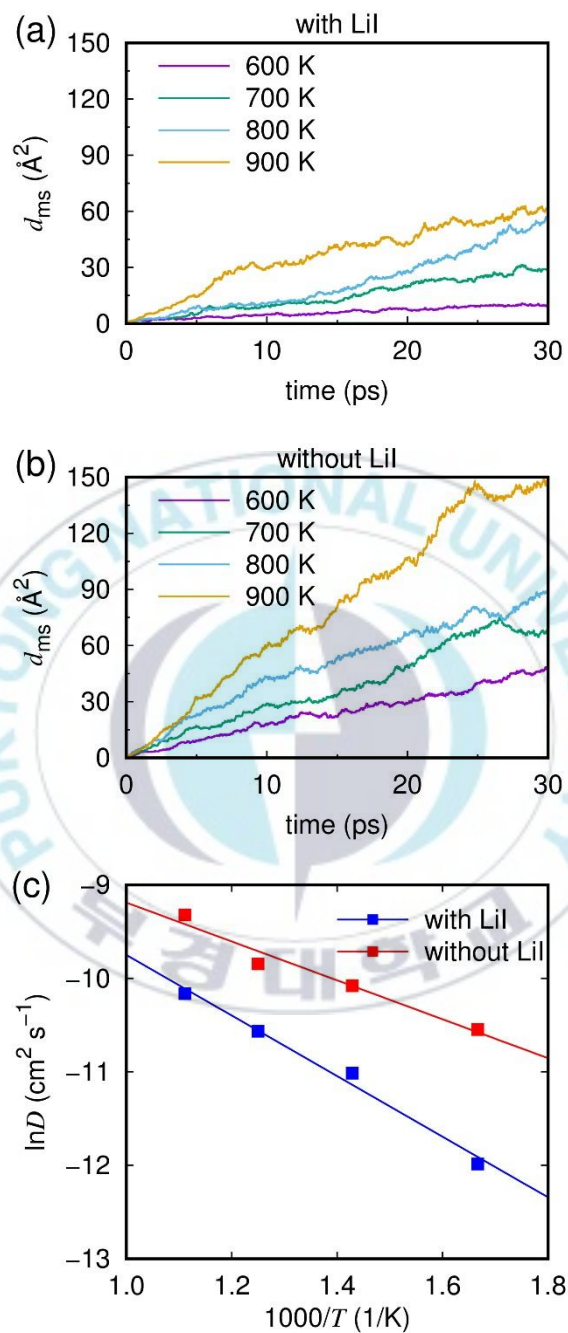


**Fig. 7.** Mean-square displacements ( $d_{ms}$ ) of Li ions in the LIBOSS ( $x = 0$ ) glasses (a) with and (b) without crystalline LiI. (c) Logarithmic diffusivities ( $\ln D$ ) of Li ions in the LIBOSS ( $x = 0$ ) glasses with and without crystalline LiI.

#### 4.4. Bader charge and diffusion trajectory

Two factors can explain why the LIBOSS glass with  $x = 0.25$  has the highest Li ion conductivity. First, the higher conductivity at  $x = 0.25$  than at  $x = 0$  is due to the absence of LiI crystals in the LIBOSS glass. Li ions in LiI crystals hardly participate in ion transport because they are almost immobile. Indeed, at  $x = 0$ , LIBOSS glass without crystalline LiI exhibits a diffusivity of  $7.9 \times 10^{-7} \text{ cm}^2 \text{ s}^{-1}$  and a conductivity of  $66.1 \text{ mS cm}^{-1}$  (Table 3 and Figure 7). These values are higher than for LIBOSS glass with  $x = 0.25$  ( $2.0 \times 10^{-7} \text{ cm}^2 \text{ s}^{-1}$  and  $14.6 \text{ mS cm}^{-1}$ , respectively). Second, the higher conductivity at  $x = 0.25$  than at  $x = 0.5$  and  $1.0$  is because  $C_{\text{N}_{\text{Li-O}}}$  increases as  $x$  increases from  $0.25$  to  $1.0$  (Fig. 3). Diffused Li ions can exhibit attractive interactions with anions that are O, S and I and repulsive interactions with Li, B and Si cations. The Li-A electrostatic interaction (A = Li, B, O, Si, S, I) can be estimated by a simple method using the Li-A distance ( $d$ ) of A and the Bader charge ( $Q$ ). The electrostatic energy term ( $-Q_{\text{Li}}Q_{\text{A}}/d_{\text{Li-A}}$ ) estimated at  $x = 0.25$  shows that the attractive interaction strength of Li-A decreases in the order Li-O > Li-S > Li-I, and the repulsive interaction strength is Li-B > Li-Si > Li-I in the order of decreasing (Table 4).

**Table 4**

Li–A distances ( $d$ ), Bader charges ( $Q$ ), and their combinations to evaluate the electrostatic interactions in the LIBOSS ( $\text{Li}_{1.05}\text{B}_{0.5}\text{Si}_x\text{O}_{2x}\text{S}_{1.05}\text{I}_{0.45}$ ) glass with  $x = 0.25$ .

A	$d_{\text{Li-A}}$ (Å) <sup>a</sup>	$Q_{\text{A}}$ ( $e$ ) <sup>b</sup>	$-Q_{\text{Li}}Q_{\text{A}}/d_{\text{Li-A}}$ <sup>c</sup>
Li	3.18	+0.90	-0.26
B	2.98	+1.69	-0.51
O	1.93	-1.47	+0.69
Si	3.85	+2.03	-0.48
S	2.48	-1.09	+0.40
I	2.78	-0.64	+0.21

<sup>a</sup>The  $d_{\text{Li-A}}$  values indicate the first-peak positions of the RDFs in Fig. 2.

<sup>b</sup>The  $Q_{\text{A}}$  values were determined by averaging the Bader charges of atoms of the three structures obtained during the AIMD simulation at  $T = 300$  K.

<sup>c</sup>Units are omitted. The positive and negative signs indicate the attractive and repulsive interactions between Li and A, respectively.

Since Li ions can migrate by breaking bonds with surrounding anions, breaking the strongest Li–O bonds is essential for rapid Li ion diffusion. As shown in Fig. 3,  $CN_{Li-O}$  increases by 0.62 from 0.89 to 1.51. As  $x$  increases from 0.25 to 1.0, it can be seen that the diffusion of Li ions must break bonds with O atoms as  $x$  increases. This leads to a decrease in conductivity as the  $SiO_2$  content increases. The introduction of  $SiO_2$  into LIBOSS causes the local LiI crystals in the LIBOSS glass to decompose, increasing the number of mobile Li ions. However, as the  $SiO_2$  content increases, the movement of Li ions is increasingly hindered by O atoms, resulting in maximum conductivity at  $x = 0.25$ . The way in which individual Li ions diffuse in the LIBOSS glass was also investigated. Fig. 8(a) shows the  $d_{ms}$  curves of fast and slow moving Li ions obtained from AIMD simulations of LIBOSS glass with  $x = 0.25$  at  $T = 900$  K. The  $d_{ms}$  value of slow Li ions is less than  $50 \text{ \AA}^2$ , whereas the  $d_{ms}$  value of fast Li ions is up to  $300 \text{ \AA}^2$ . The values of  $CN_{Li-A}$  ( $A = Li, B, O, Si, S, I$ ) calculated for slow Li ions and fast Li ions show that the total number of cations around Li ( $CN_{Li-cation}$ ) equals the total number of anions around Li. ( $CN_{Li-anion}$ ) is smaller than (Fig. 8(b)). Interestingly, the  $CN_{Li-anion}$  of the fast Li ion (4.08) is greater than the  $CN_{Li-positivity}$  of the slow Li ion (4.06) by 0.69 than that of the slow Li ion (2.88). It has a higher cation to anion ratio for fast Li ions (0.88) than for slow Li ions (0.71).

The presence of many cations around Li seems to be an important factor for the rapid diffusion of Li ions. As mentioned earlier, Li ions can diffuse by

breaking their bonds with surrounding anions, especially oxygen, which attracts the Li ions the most. If only anions exist around Li ions, it is very difficult for the anions to diffuse due to the strong Li-anion bond. However, when both cations and anions surround Li ions, the bond between Li ions and anions is weakened because the cations attract the anions. This provides more opportunities for Li ions to break their bonds with the nearest anions and escape. To confirm this, the values of  $CN_{Li-A}$  and  $d_{Li-A}$  for fast Li ions in Fig. 8(a) were analyzed over a period of 13.1 to 14.1 ps in which the dms curve rapidly increased (inset of Fig. 8(a)). See Part A and B). This 1ps period corresponds to a hopping event in the Li diffusion process, which is a repetition of Li ion oscillation and hopping, as in the fast Li ion orbit in Fig. 8(c). The calculated  $CN_{Li-A}$  and  $d_{Li-A}$  values over 1 and 30 ps periods are presented in Table 5. The  $CN_{Li-A}$  values for the 1-ps period are 0.22–1.63 smaller than that for the 30-ps period, whereas  $CN_{Li-Si}$  and  $CN_{Li-S}$  are 0.02 and 0.73 greater than the 30-ps period, respectively. Therefore,  $CN_{Li-cation}$  and  $CN_{Li-anion}$  in 1-ps period are 2.25 and 0.17, respectively, which are smaller than  $CN_{Li-cation}$  in 30-ps period. The  $d_{Li-A}$  values in the 1-ps period are 0.11–0.69 Å longer than those in the 30-ps period, except for A = S and I. The  $d_{Li-S}$  value of the 1-ps period is the same as that of the 30-ps period, and the  $d_{Li-I}$  value of the 1-ps period is 0.04 Å shorter than the value of the 30-ps period. Comparing  $CN_{Li-A}$  and  $d_{Li-A}$  with 1-ps and 30-ps periods, it can be seen that Li ions can jump at the moment they are attracted by cations. In particular, during hopping of Li ions,  $d_{Li-O}$  increased

significantly by 0.69 Å from 2.09 Å (30 ps) to 2.78 Å (1 ps), indicating that breaking Li–O bonds is very important for Li–O hopping. . During Li ion hopping,  $CN_{Li-O}$  decreases by 0.68 from 0.68 (30 ps) to 0.003 (1 ps), while  $CN_{Li-S}$  increases by 0.73 from 1.51 (30 ps) to 2.24 (1 ps). During Li ion hopping,  $CN_{Li-O}$  decreases by 0.68 from 0.68 (30 ps) to 0.003 (1 ps), while  $CN_{Li-S}$  increases by 0.73 from 1.51 (30 ps) to 2.24 (1 ps). This suggests that, unlike O atoms, S atoms do not inhibit Li ion hopping, which is consistent with higher Li ion conductivity in sulfides than in oxide solid electrolytes. As shown in Figure 8 and Table 5, when the Li–anionic bond is weakened with the help of surrounding cations, Li ions can easily jump, which can be viewed as cation-assisted Li ion diffusion.

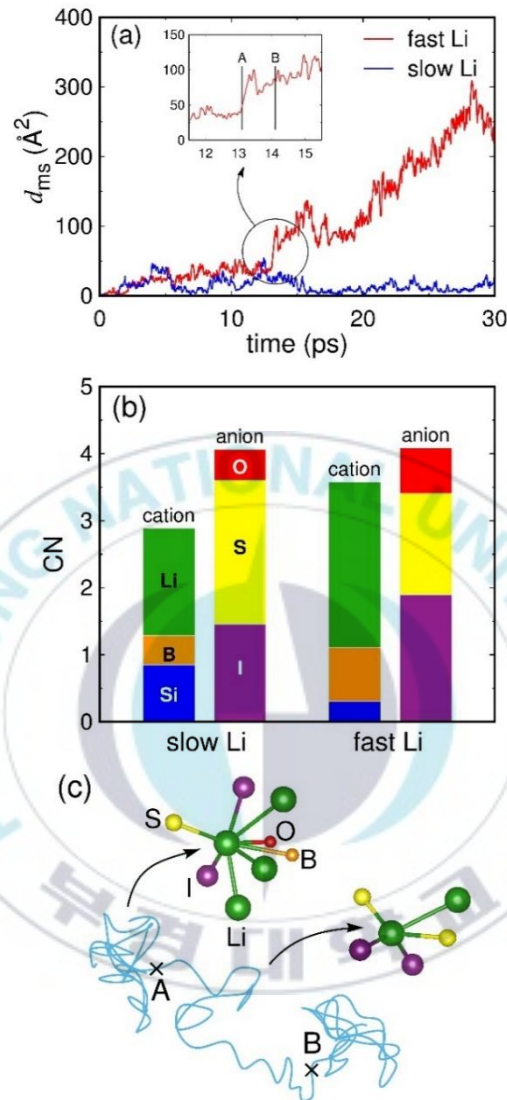


**Fig. 8.** (a) Mean-square displacements ( $d_{ms}$ ) of fast- and slow-moving Li ions in the LIBOSS ( $\text{Li}_{1.05}\text{B}_{0.5}\text{Si}_x\text{O}_{2x}\text{S}_{1.05}\text{I}_{0.45}$ ) glass with  $x = 0.25$  at  $T = 900$  K. (b) Coordination numbers (CNs) of the fast and slow Li ions over a period of 30 ps. (c) Trajectory of the fast Li ion over a period of 4 ps (11.5–15.5 ps). A and B represent 13.1 and 14.1 ps, respectively. The atomic configurations at 12.7 and 13.6 ps are displayed.

**Table 5**

$CN_{Li-A}$  and  $d_{Li-A}$  of the fast Li ion in Fig. 8(a), obtained over a partial period of 1 ps (13.1–14.1 ps) and a full period of 30 ps in the AIMD simulation of the LIBOSS ( $Li_{1.05}B_{0.5}Si_xO_{2x}S_{1.05}I_{0.45}$ ) glass with  $x = 0.25$  for 30 ps at  $T = 900$  K.

	cation				anion			
	A	1 ps	30 ps	$\Delta$	A	1 ps	30 ps	$\Delta$
$CN_{Li-A}$	Li	0.84	2.47	-1.63	O	0.003	0.68	-0.68
	B	0.16	0.80	-0.64	S	2.24	1.51	+0.73
	Si	0.32	0.30	+0.02	I	1.67	1.89	-0.22
	total	1.32	3.57	-2.25	total	3.91	4.08	-0.17
$d_{Li-A}$ (Å)	Li	3.40	3.23	+0.17	O	2.78	2.09	+0.69
	B	3.03	2.92	+0.11	S	2.66	2.66	0.00
	Si	3.27	3.11	+0.16	I	2.94	2.98	-0.04

#### 4.5. H<sub>2</sub>S gas formation

Kaup et al. also reported that the production of H<sub>2</sub>S is reduced when adding oxygen to LIBOSS [22]. Our calculations show that SiO<sub>2</sub> in LIBOSS increases the resistance to H<sub>2</sub>S gas formation. When the LIBOSS glass reacted with H<sub>2</sub>O, the H<sub>2</sub>S formation reaction was assumed to be as follows: LIBOSS(N<sub>S</sub>) (s) + 2H<sub>2</sub>O (g) → LIBOSS(N<sub>S</sub> - 2) (s) + 2H<sub>2</sub>S (g) + O<sub>2</sub> (g), where N<sub>S</sub> represents the number of S atoms in the supercell and s and g represent solid and gas phases, respectively. The LIBOSS(N<sub>S</sub> - 2) structure was obtained by optimizing the LIBOSS structure in which two S atoms were removed, and several LIBOSS(N<sub>S</sub> - 2) structures were investigated to calculate the formation energy of H<sub>2</sub>S. The calculated average H<sub>2</sub>S formation energies are 3.20 and 3.94 eV at  $x = 0$  and 0.25, respectively (Fig. 6), indicating that H<sub>2</sub>S formation is not energetically good at  $x = 0.25$  than at  $x = 0$ .

The roles of oxygen and sulfur in glassy solid electrolytes can be summarized from our calculation results as follows: oxygen reduces immobilized Li ions (i.e., kinetically lost Li ions) and inhibits H<sub>2</sub>S formation but hinders Li ion diffusion, whereas sulfur relatively promotes Li ion diffusion but causes H<sub>2</sub>S formation. It is thus preferable that glassy solid electrolytes contain both oxygen and sulfur. Furthermore, precise control of the oxygen:sulfur ratio is key to

achieving optimal performance of the glassy solid electrolyte in terms of conductivity and moisture stability.



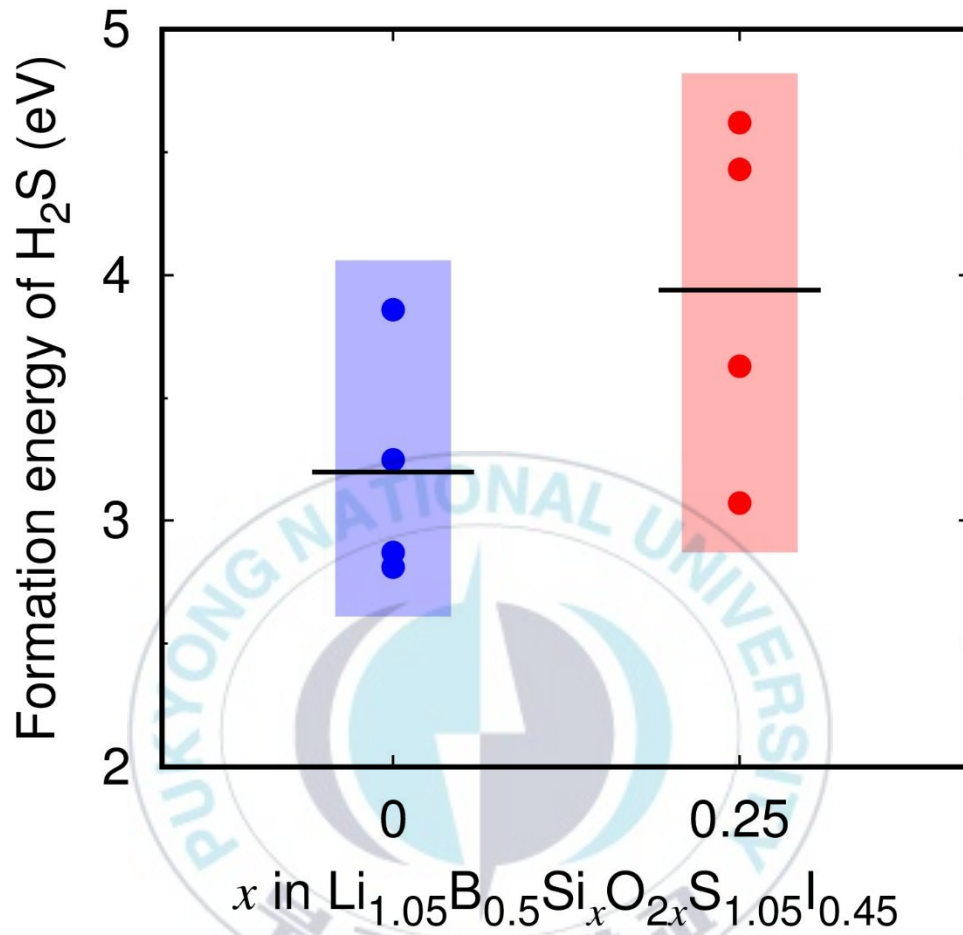


**Fig. 9.** Formation energy of H<sub>2</sub>S from LIBOSS, defined as  $E_f = [E(\text{LIBOSS}; N_S - 2) + 2E(\text{H}_2\text{S}) + 2E(\text{O}_2) - E(\text{LIBOSS}; N_S) - 2E(\text{H}_2\text{O})]/2$ , where  $E(\text{LIBOSS})$  is the energy of LIBOSS glass, and  $E(\text{H}_2\text{S})$ ,  $E(\text{O}_2)$ , and  $E(\text{H}_2\text{O})$  are the energies of H<sub>2</sub>S, O<sub>2</sub>, and H<sub>2</sub>O molecules, respectively. The positive formation energy indicates that the formation of H<sub>2</sub>S from LIBOSS is energetically unfavorable. Horizontal bars represent the average formation energies.

## 5. Conclusion

This first-principle study elucidated the diffusion mechanism of Li ions inside LIBOSS ( $\text{Li}_{1.05}\text{B}_{0.5}\text{Si}_x\text{O}_{2x}\text{S}_{1.05}\text{I}_{0.45}$ ) glasses. Oxygen in the LIBOSS glass exerts two opposing effects, respectively, which degrade local LiI crystals and strongly attract Li ions, increasing and decreasing Li ion conductivity. Between the two effects of oxygen, the maximum conductance reached  $14.6 \text{ mS cm}^{-1}$  when  $\text{SiO}_2$  was added by  $x = 0.25$ . Li ions can diffuse much faster in a cation-rich environment than in a cation-poor environment, because the cation attracts anions around Li, so the Li ions can break bonds with surrounding anions, especially oxygen. Our work provides an atomic-level understanding of ion transport in glass materials as well as the roles of glass elements in terms of conductivity, salt decomposition, and hydrogen sulfide formation. The proposed cation-assisted ion diffusion mechanism and the elucidated roles of oxygen and sulfur could be helpful in designing high-performance glassy solid electrolytes for ASSBs.

## References

- [1] Y. Gao, Z. Yan, J.L. Gray, X. He, D. Wang, T. Chen, Q. Huang, Y.C. Li, H. Wang, S.H. Kim, T.E. Mallouk, D. Wang, Polymer–inorganic solid–electrolyte interphase for stable lithium metal batteries under lean electrolyte conditions, *Nat. Mater.* 18 (2019) 384–389.
- [2] X. Chen, W. He, L.X. Ding, S. Wang, H. Wang, Enhancing interfacial contact in all solid state batteries with a cathode-supported solid electrolyte membrane framework, *Energy Environ. Sci.* 12 (2019) 938–944.
- [3] J.W. Fergus, Ceramic and polymeric solid electrolytes for lithium-ion batteries, *J. Power Sources.* 195 (2010) 4554–4569.
- [4] C. Lai, C. Shu, W. Li, L. Wang, X. Wang, T. Zhang, X. Yin, I. Ahmad, M. Li, X. Tian, P. Yang, W. Tang, N. Miao, G.W. Zheng, Stabilizing a Lithium Metal Battery by an in Situ  $\text{Li}_2\text{S}$ -modified Interfacial Layer via Amorphous-Sulfide Composite Solid Electrolyte, *Nano Lett.* 20 (2020) 8273–8281.
- [5] S. Kaboli, H. Demers, A. Paoletta, A. Darwiche, M. Dontigny, D. Clément, A. Guerfi, M.L. Trudeau, J.B. Goodenough, K. Zaghib, Behavior of Solid Electrolyte in Li-Polymer Battery with NMC Cathode via in-Situ Scanning Electron Microscopy, *Nano Lett.* 20 (2020) 1607–1613.
- [6] T. Famprikis, P. Canepa, J.A. Dawson, M.S. Islam, C. Masquelier,

- Fundamentals of inorganic solid-state electrolytes for batteries, *Nat. Mater.* 18 (2019) 1278–1291.
- [7] Q. Wang, L. Jiang, Y. Yu, J. Sun, Progress of enhancing the safety of lithium ion battery from the electrolyte aspect, *Nano Energy.* 55 (2019) 93–114.
- [8] L. Han, C. Liao, X. Mu, N. Wu, Z. Xu, J. Wang, L. Song, Y. Kan, Y. Hu, Flame-Retardant ADP/PEO Solid Polymer Electrolyte for Dendrite-Free and Long-Life Lithium Battery by Generating Al, P-rich SEI Layer, *Nano Lett.* 21 (2021) 4447–4453.
- [9] H. Chen, D. Adekoya, L. Hencz, J. Ma, S. Chen, C. Yan, H. Zhao, G. Cui, S. Zhang, Stable Seamless Interfaces and Rapid Ionic Conductivity of Ca–CeO<sub>2</sub>/LiTFSI/PEO Composite Electrolyte for High-Rate and High-Voltage All-Solid-State Battery, *Adv. Energy Mater.* 10 (2020) 1–13.
- [10] Z. Wu, Z. Xie, A. Yoshida, Z. Wang, X. Hao, A. Abudula, G. Guan, Utmost limits of various solid electrolytes in all-solid-state lithium batteries: A critical review, *Renew. Sustain. Energy Rev.* 109 (2019) 367–385.
- [11] R. Pathak, K. Chen, A. Gurung, K.M. Reza, B. Bahrami, J. Pokharel, A. Baniya, W. He, F. Wu, Y. Zhou, K. Xu, Q. (Quinn) Qiao, Fluorinated hybrid solid-electrolyte-interphase for dendrite-free lithium deposition, *Nat. Commun.* 11 (2020) 1–10.
- [12] W. Zhang, J. Nie, F. Li, Z.L. Wang, C. Sun, A durable and safe solid-state lithium battery with a hybrid electrolyte membrane, *Nano Energy.*

45 (2018) 413–419.

- [13] Y. Seino, T. Ota, K. Takada, A. Hayashi, M. Tatsumisago, A sulphide lithium super ion conductor is superior to liquid ion conductors for use in rechargeable batteries, *Energy Environ. Sci.* 7 (2014) 627–631.
- [14] N. Kamaya, K. Homma, Y. Yamakawa, M. Hirayama, R. Kanno, M. Yonemura, T. Kamiyama, Y. Kato, S. Hama, K. Kawamoto, A. Mitsui, A lithium superionic conductor, *Nat. Mater.* 10 (2011) 682–686.
- [15] Y. Kato, S. Hori, T. Saito, K. Suzuki, M. Hirayama, A. Mitsui, M. Yonemura, H. Iba, R. Kanno, High-power all-solid-state batteries using sulfide superionic conductors, *Nat. Energy.* 1 (2016) 1–7.
- [16] K. Takada, Progress and prospective of solid-state lithium batteries, *Acta Mater.* 61 (2013) 759–770.
- [17] S.Y. Jung, R. Rajagopal, K.S. Ryu, Synthesis and electrochemical performance of  $(100-x)\text{Li}_7\text{P}_3\text{S}_{11-x}\text{Li}_2\text{OHBr}$  composite solid electrolyte for all-solid-state lithium batteries, *J. Energy Chem.* 47 (2020) 307–316.
- [18] A. Manthiram, X. Yu, S. Wang, Lithium battery chemistries enabled by solid-state electrolytes, *Nat. Rev. Mater.* 2 (2017) 1–16.
- [19] A. Baktash, J.C. Reid, Q. Yuan, T. Roman, D.J. Searles, Shaping the Future of Solid-State Electrolytes through Computational Modeling, *Adv. Mater.* 32 (2020) 1–7.
- [20] J. Zhang, C. Zheng, J. Lou, Y. Xia, C. Liang, H. Huang, Y. Gan, X. Tao, W. Zhang, Poly(ethylene oxide) reinforced  $\text{Li}_6\text{PS}_5\text{Cl}$  composite solid electrolyte for all-solid-state lithium battery: Enhanced electrochemical

- performance, mechanical property and interfacial stability, *J. Power Sources*. 412 (2019) 78–85.
- [21] A. Hayashi, H. Muramatsu, T. Ohtomo, S. Hama, M. Tatsumisago, Improvement of chemical stability of  $\text{Li}_3\text{PS}_4$  glass electrolytes by adding  $\text{M}_x\text{O}_y$  (M = Fe, Zn, and Bi) nanoparticles, *J. Mater. Chem. A*. 1 (2013) 6320–6326.
- [22] K. Kaup, J.D. Bazak, S.H. Vajargah, X. Wu, J. Kulisch, G.R. Goward, L.F. Nazar, A Lithium Oxythioborosilicate Solid Electrolyte Glass with Superionic Conductivity, *Adv. Energy Mater.* 10 (2020) 1–9.
- [23] R. Zhao, S. Kmiec, G. Hu, S.W. Martin, Lithium Thiosilicophosphate Glassy Solid Electrolytes Synthesized by High-Energy Ball-Milling and Melt-Quenching: Improved Suppression of Lithium Dendrite Growth by Si Doping, *ACS Appl. Mater. Interfaces*. 12 (2020) 2327–2337.
- [24] L. Katzenmeier, S. Helmer, S. Braxmeier, E. Knobbe, A.S. Bandarenka, Properties of the Space Charge Layers Formed in Li-Ion Conducting Glass Ceramics, *ACS Appl. Mater. Interfaces*. 13 (2021) 5853–5860.
- [25] Z. Wang, Y. Jiang, J. Wu, Y. Jiang, W. Ma, Y. Shi, X. Liu, B. Zhao, Y. Xu, J. Zhang, Doping effects of metal cation on sulfide solid electrolyte/lithium metal interface, *Nano Energy*. 84 (2021) 105906.
- [26] G. Zhou, X. Lin, J. Liu, J. Yu, J. Wu, H.M. Law, Z. Wang, F. Ciucci, In situ formation of poly(butyl acrylate)-based non-flammable elastic quasi-solid electrolyte for dendrite-free flexible lithium metal batteries with long cycle life for wearable devices, *Energy Storage Mater.* 34 (2021)

629–639.

- [27] S.K. Jung, H. Gwon, G. Yoon, L.J. Miara, V. Lacivita, J.S. Kim, Pliable Lithium Superionic Conductor for All-Solid-State Batteries, *ACS Energy Lett.* 6 (2021) 2006–2015.
- [28] F. Han, J. Yue, X. Zhu, C. Wang, Suppressing Li Dendrite Formation in  $\text{Li}_2\text{S-P}_2\text{S}_5$  Solid Electrolyte by LiI Incorporation, *Adv. Energy Mater.* 8 (2018) 6–11.
- [29] F. Wu, W. Fitzhugh, L. Ye, J. Ning, X. Li, Advanced sulfide solid electrolyte by core-shell structural design, *Nat. Commun.* 9 (2018) 1–11.
- [30] Y. Shao, G. Zhong, Y. Lu, L. Liu, C. Zhao, Q. Zhang, Y.S. Hu, Y. Yang, L. Chen, A novel NASICON-based glass-ceramic composite electrolyte with enhanced Na-ion conductivity, *Energy Storage Mater.* 23 (2019) 514–521.
- [31] X. Feng, P.H. Chien, S. Patel, J. Zheng, M. Immediato-Scuotto, Y. Xin, I. Hung, Z. Gan, Y.Y. Hu, Synthesis and characterizations of highly conductive and stable electrolyte  $\text{Li}_{10}\text{P}_3\text{S}_{12}\text{I}$ , *Energy Storage Mater.* 22 (2019) 397–401.
- [32] E. Fermi, Eine statistische Methode zur Bestimmung einiger Eigenschaften des Atoms und ihre Anwendung auf die Theorie des periodischen Systems der Elemente, *Zeitschrift Für Phys.* 48 (1928) 73–79.
- [33] J.P. Perdew, J.A. Chevary, S.H. Vosko, K.A. Jackson, M.R. Pederson, D.J. Singh, C. Fiolhais, Erratum: Atoms, molecules, solids, and surfaces:

Applications of the generalized gradient approximation for exchange and correlation (Physical Review B (1993) 48, 7, (4978)), Phys. Rev. B. 48 (1993) 4978.

- [34] J.P. Perdew, K. Burke, M. Ernzerhof, Generalized gradient approximation made simple, Phys. Rev. Lett. 77 (1996) 3865–3868.
- [35] D.C. Langreth, M.J. Mehl, Beyond the local-density approximation in calculations of ground-state electronic properties, Phys. Rev. B. 28 (1983) 1809–1834.
- [36] D.R. Hamann, M. Schlüter, C. Chiang, Norm-Conserving Pseudopotentials, Phys. Rev. Lett. 43 (1979) 1494–1497.
- [37] P.E. Blöchl, Projector augmented-wave method, Phys. Rev. B. 50 (1994) 17953–17979.
- [38] G. Kresse, Efficient iterative schemes for ab initio total-energy calculations using a plane-wave basis set, Phys. Rev. B. 54 (1996) 11169.
- [39] P. Pulay, Convergence acceleration of iterative sequences. the case of scf iteration, Chem. Phys. Lett. 73 (1980) 393–398.
- [40] M. Ménétrier, C. Estournès, A. Levasseur, K.J. Rao, Ionic conduction in  $B_2S_3-Li_2S-LiI$  glasses, Solid State Ionics. 53–56 (1992) 1208–1213.
- [41] P. Vinatier, M. Ménétrier, A. Levasseur, Aggregation of the doping salt in  $B_2S_3-Li_2S-LiI$  glasses, effect on the dynamical properties, Solid State Ionics. 116 (1999) 35–45.

## Publications

G.H. Cha, S.C. Jung, Cation-Assisted Lithium Ion Diffusion in a Lithium Oxythioborate Halide Glass Solid Electrolyte, *Electrochim. Acta* (accepted).

## Conferences

G.H. Cha, S. C. Jung, First-Principles Study of Li-Ion Conduction in Lithium Oxythioborate Halide Glasses, *Bull. of Kor. Phys. Soc. Busan-Ulsan-Gyeongnam Branch*, 43, No. 71 (2021, Korea).

G. H. Cha, S. C. Jung, Fast Ion Conduction Mechanism of Lithium Oxythioborate Halide Glass Solid electrolyte, *Bull. of International Conference on Advanced Materials and Devices*, 1095, No. 12 (2021, Korea).

## Awards

Best poster presentation award, G.H. Cha, S. C. Jung, *Kor. Phys. Soc. Busan-Ulsan-Gyeongnam Branch* (2021, Korea).

## 감사의 글

길다고 생각했던 2년 간의 석사 과정이 벌써 끝맺음을 맺으려 하고 있습니다. 하지만 저는 아직 부족한 부분이 많아 석사과정이 끝나는 것이 매우 아쉽게 느껴지는 것 같습니다. 미흡한 부분이 많은 저이지만 감사하게도 학위 논문을 마치기까지 많은 분들이 도움을 주셨기에 이 자리를 빌어 감사의 말씀을 드리고자 합니다.

먼저 연구에 대해 많은 조언과 지적, 문제에 대한 해결책을 지도해주신 지도 교수님, 정성철 교수님께 진심을 담아 감사의 말을 드립니다. 학부 때부터 현재까지 언제나 연구자로서의 마음가짐을 알려주셨지만 아직 미흡한 부분이 많은 것 같습니다. 계산 결과에서 의미를 찾지 못할 때 무엇이 부족하고 무엇이 필요한지 꼼꼼하게 조언 해주신 덕분에 졸업이라는 결실을 맺을 수 있었습니다. 다시 한번 감사의 말씀을 드립니다.

또 바쁘신 와중에 본 논문을 위한 날카로운 지적과 저에게 따뜻한 조언을 해주신 홍지상 교수님과 이보람 교수님께도 감사의 말씀을 드리고 싶습니다.

그리고 실무적으로 많은 부분을 가르쳐주고 연구실 생활에서 많은 도움을 주신 전태곤 선배님께도 감사를 전하고 싶습니다. 아울러 대학원 생활 동안 학문적이든 학문적이지 않든 여러 생각을 주고 받았던 이영철, 김기석, 광승엽 등 동기들에게 고맙다는 말을 전하고 싶습니다.

마찬가지로 사회생활 중에도 연락하며 여러 도움을 준 문진홍 외 7명에게도 고마움을 전합니다.

마지막으로 저를 언제나 믿어주시고 힘들 때에도 정신적으로 지탱 해주신 부모님과 누나와 친인척 모두에게 감사의 인사를 드립니다. 모두의 진심 어린 격려와 조언 덕분에 여기까지 도달할 수 있었던 것 같습니다. 다시 한번 감사의 마음을 전합니다.

벌써 20대의 후반부를 지나고 있는 저는 미숙하고 미흡하지만 많은 분들

의 도움을 통해 적어도 지금보다 조금 더 성장할 수 있도록 노력해보겠습니다. 부족하지만 2년간의 노력이 담긴 이 논문을 바칩니다. 감사합니다.

2022년 8월  
차경호

